On the Role of the Influence Function in the Peridynamic Theory

Pablo Seleson* and Michael L. Parks†‡

Abstract

The influence function in the peridynamic theory is used to weight the contribution of all the bonds participating in the computation of volume-dependent properties. In this work, we use influence functions to establish relationships between bond-based and state-based peridynamic models. We also demonstrate how influence functions can be used to modulate nonlocal effects within a peridynamic model independently of the peridynamic horizon. We numerically explore the effects of influence functions by studying wave propagation in simple one-dimensional models and brittle fracture in three-dimensional models.

Key Words: *Peridynamics, influence function, nonlocal*

1 Introduction

The peridynamic theory was first proposed in Silling (2000) as a nonlocal extension of classical continuum mechanics, and is a member of a larger class of nonlocal continuum mechanics theories (see, e.g., Kröner (1967), Kunin (1982, 1983), Rogula (1982), Eringen (2002), and the references cited therein). A central characteristic of peridynamic models is an absence of spatial derivatives of field quantities. In a peridynamic model, internal interactions between points within a body are calculated via integrals involving differences, not derivatives. The consequences of this formulation are twofold.

First, like all nonlocal models, peridynamic models possess length scales and are thus suitable for multiscale modeling (Askari et al. (2008)). As a multiscale model, peridynamics can be interpreted as an upscaling of molecular dynamics (Seleson et al. (2009)), allowing a transition from atomistic to macroscopic length scales. Further, the peridynamic horizon (see (2.1)) can be matched to the dominant length scale of material inhomogeneities, enabling multiscale modeling for complex materials such as composite laminates (Alali (2008)). Also, a local/nonlocal coupling method based upon domain decomposition theory has been developed to allow simultaneous coupled simulations with peridynamic models and classical models (Seleson et al. (2010)).

Second, owing to their formulation based upon integrals of differences instead of derivatives, peridynamic models admit a larger class of solutions than corresponding classical (local) models. As a prime example, peridynamic solid mechanics models admit discontinuous displacement fields, even in their strong forms, making them suitable for modeling material failure and fracture (Ha and Bobaru (2010)). Mathematical investigations of the peridynamic theory have lead to the development of a nonlocal calculus (Gunzburger and Lehoucq (2010)), rigorous analysis of peridynamic operators (Zhou and Du (2010), Du and Zhou (2010), Emmrich and Weckner (2007)), and development of the first nonlocal domain decomposition theory (Aksoylu and Parks (2009)).

Influence functions (see Definition 2.1) were first introduced in the modern *state-based* formulation of peridynamics (Silling et al. (2007)). Although originally utilized as Boolean-valued functions, i.e., having

*Department of Scientific Computing, 400 Dirac Science Library, Florida State University, Tallahassee, FL 32306-4120, ps06c@fsu.edu.

†Sandia National Laboratories, Applied Mathematics and Applications, P.O. Box 5800, MS 1320, Albuquerque, NM 87185-1320, mlparks@sandia.gov.

‡Sandia is a multiprogram laboratory operated by Sandia Corporation, a Lockheed Martin Company, for the United States Department of Energy under contract DE-AC04-94-AL85000.

values of 0 or 1, we will demonstrate that even simple generalizations of these functions allow one to modulate nonlocal effects within a constitutive model, permitting a rich range of dynamic behavior. In §2 we review the peridynamic theory, and focus on specific common peridynamic constitutive models and their relationships in §3. In §4 we present two simple one-dimensional models with parameterized influence functions and examine their behavior through analysis and numerical experiment. In §5 we present numerical results for fully 3D dynamic fracture simulations, showing the impact of influence functions. We offer conclusions in §6.

2 The Peridynamic Theory

In the state-based peridynamic theory, the deformation at a point depends collectively on all points interacting with that point. Using the notation of Silling et al. (2007), we write the peridynamic equation of motion as

$$\rho(\mathbf{x})\ddot{\mathbf{u}}(\mathbf{x},t) = \int_{\mathcal{H}_\mathbf{x}} \left\{\underline{\mathbf{T}}\left[\mathbf{x},t\right]\langle\mathbf{x}'-\mathbf{x}\rangle - \underline{\mathbf{T}}\left[\mathbf{x}',t\right]\langle\mathbf{x}-\mathbf{x}'\rangle\right\} dV_{\mathbf{x}'} + \mathbf{b}(\mathbf{x},t), \tag{2.1}$$

where ρ represents the mass density, $\mathbf{u}$ the displacement field, and $\mathbf{b}$ an external body force density. A point $\mathbf{x}$ interacts with all the points $\mathbf{x}'$ within the neighborhood $\mathcal{H}_\mathbf{x}$, assumed to be a spherical region of radius $\delta > 0$ centered at $\mathbf{x}$. δ is called the *horizon*, and is analogous to the cutoff radius used in molecular dynamics. The operator $\underline{\mathbf{T}}$ is the *force vector state*, explained below. Conditions on $\underline{\mathbf{T}}$ for which (2.1) satisfies balance of linear and angular momentum are given in Silling et al. (2007).

A *vector state* is an operator whose image is a vector and may be viewed as a generalization of a second-order tensor. Similarly, a *scalar state* is an operator whose image is a scalar. As such, the force vector state $\underline{\mathbf{T}}\left[\mathbf{x},t\right]\langle\cdot\rangle$ is a mapping, having units of force per volume squared, of the vector $\mathbf{x}'-\mathbf{x}$ to the force vector state field. Note that the constitutive model is completely contained within $\underline{\mathbf{T}}$. See Silling et al. (2007) for a complete discussion of states.

The vector $\mathbf{x}'-\mathbf{x}$ is referred to as the *bond* between the points $\mathbf{x}$ and $\mathbf{x}'$. Let $\mathbf{u}(\mathbf{x},t)$ and $\mathbf{y}(\mathbf{x},t)$ denote the displacement and position, respectively, of the point $\mathbf{x}$ at time t. In the following, we will utilize the notation $\boldsymbol{\xi} := \mathbf{x}'-\mathbf{x}$ to denote the relative position of two particles in the reference configuration (i.e., the bond in the reference configuration). We will denote the relative displacement of two points as $\boldsymbol{\eta} := \mathbf{u}(\mathbf{x}',t)-\mathbf{u}(\mathbf{x},t)$, such that the relative position in the current configuration is $\boldsymbol{\xi}+\boldsymbol{\eta} = \mathbf{y}(\mathbf{x}',t)-\mathbf{y}(\mathbf{x},t)$, i.e., the bond in the current configuration.

We now define an influence function following Definition 3.2 in Silling et al. (2007).

Definition 2.1 *An influence function is a nonnegative scalar state $\underline{\omega}$ defined on $\mathcal{H}$. If an influence function $\underline{\omega}$ depends only upon the scalar $||\boldsymbol{\xi}||$, i.e., $\underline{\omega}\langle\boldsymbol{\xi}\rangle = \underline{\omega}\langle||\boldsymbol{\xi}||\rangle$, then $\underline{\omega}$ is a spherical influence function.*

Influence functions are used in the construction of peridynamic constitutive models (see §3).

In Silling et al. (2007), influence functions were suggested as a selection mechanism to determine which bonds participate in the calculation of the force state and other related quantities. Bonds may be removed from the force state calculation as a simulation proceeds, for example, if they are broken. This particular use of Boolean-valued influence functions was presented in Foster et al. (2010). We will show that the influence functions can also be used to connect related families of peridynamic constitutive models and to modulate the strength of a nonlocal interaction.

In this paper, we will consider only spherical influence functions. Also, we will consider only force vector states that can be written as

$$\underline{\mathbf{T}} = \underline{t}\,\underline{\mathbf{M}}$$

with $\underline{t}$ a *force scalar state* and $\underline{\mathbf{M}}$ the *deformed direction vector state* defined by

$$\underline{\mathbf{M}}\langle\boldsymbol{\xi}\rangle = \begin{cases} \dfrac{\boldsymbol{\xi}+\boldsymbol{\eta}}{||\boldsymbol{\xi}+\boldsymbol{\eta}||} & ||\boldsymbol{\xi}+\boldsymbol{\eta}|| \neq 0, \\ \mathbf{0} & \text{otherwise.} \end{cases} \tag{2.2}$$

Such force states correspond to so-called *ordinary* materials (Silling et al. (2007)).

2.1 Peridynamic Force States Derived from Pairwise Potentials

Conservative forces derive from a potential. If we assume a force state derives from a pairwise potential (as opposed to a multibody potential), it can be written as using the force scalar state field

$$\underline{t}\left[\mathbf{x},t\right]\langle\boldsymbol{\xi}\rangle = \frac{1}{2}f(\boldsymbol{\eta},\boldsymbol{\xi}) \tag{2.3}$$

with f a scalar-valued function. Then, (2.1) reduces to

$$\rho(\mathbf{x})\ddot{\mathbf{u}}(\mathbf{x},t) = \int_{\mathcal{H}} \mathbf{f}(\boldsymbol{\eta},\boldsymbol{\xi})dV_{\boldsymbol{\xi}} + \mathbf{b}(\mathbf{x},t) \tag{2.4}$$

with

$$\mathbf{f}(\boldsymbol{\eta},\boldsymbol{\xi}) = f(\boldsymbol{\eta},\boldsymbol{\xi})\frac{\boldsymbol{\xi}+\boldsymbol{\eta}}{||\boldsymbol{\xi}+\boldsymbol{\eta}||}.$$

Equation (2.4) is the equation of motion corresponding to the *bond-based* peridynamic theory presented in Silling (2000), where $\mathbf{f}$ is called the *pairwise force function* and may be expressed as the gradient of a *pairwise potential* or *micropotential* w,

$$\mathbf{f}(\boldsymbol{\eta},\boldsymbol{\xi}) = \frac{\partial w}{\partial \boldsymbol{\eta}}(\boldsymbol{\eta},\boldsymbol{\xi}), \tag{2.5}$$

having units of energy per volume squared. We define the *macroelastic energy density* $W(\mathbf{x},t)$, at any point $\mathbf{x}$ in the body at time t, as

$$W(\mathbf{x},t) = \frac{1}{2}\int_{\mathcal{H}} w(\boldsymbol{\eta},\boldsymbol{\xi})dV_{\boldsymbol{\xi}}.$$

A consequence of using only pairwise potentials is that the resulting material models have a Poisson's ratio of $\nu = 1/4$ in 3D and $\nu = 1/3$ in 2D (Love (1944)).

3 Peridynamic Constitutive Models and Their Relationships

Two of the most commonly used peridynamic constitutive models are the *linear peridynamic solid* (LPS) model (Silling et al. (2007)) and the *prototype microelastic brittle* (PMB) model (Silling and Askari (2005)). In this section, we will show that the PMB model can be derived from the LPS model with a particular choice of influence function.

We begin with the LPS model, which represents an ordinary material with force scalar state

$$\underline{t} = \frac{3K\theta}{m}\underline{\omega}\,\underline{x} + \alpha\underline{\omega}\,\underline{e}^{\mathrm{d}}. \tag{3.1}$$

The different components of the model are described as follows. Let $\underline{x}$ be a scalar state defined by $\underline{x}\langle\boldsymbol{\xi}\rangle = ||\boldsymbol{\xi}||$. Then, the *weighted volume* m is defined as

$$m\left[\mathbf{x}\right] = \int_{\mathcal{H}} \underline{\omega}\langle\boldsymbol{\xi}\rangle\,\underline{x}\langle\boldsymbol{\xi}\rangle\,\underline{x}\langle\boldsymbol{\xi}\rangle\,\underline{x}\langle\boldsymbol{\xi}\rangle\,dV_{\boldsymbol{\xi}}.$$

Let

$$\underline{e}\left[\mathbf{x},t\right]\langle\boldsymbol{\xi}\rangle = ||\boldsymbol{\xi}+\boldsymbol{\eta}|| - ||\boldsymbol{\xi}||$$

be the *extension scalar state* and

$$\theta\left[\mathbf{x},t\right] = \frac{3}{m\left[\mathbf{x}\right]}\int_{\mathcal{H}} \underline{\omega}\langle\boldsymbol{\xi}\rangle\,\underline{x}\langle\boldsymbol{\xi}\rangle\,\underline{e}\left[\mathbf{x},t\right]\langle\boldsymbol{\xi}\rangle\,dV_{\boldsymbol{\xi}}$$

be the *dilatation*. The *isotropic* and *deviatoric* parts of the extension scalar state are defined, respectively, as

$$\underline{e}^{\mathrm{i}} = \frac{\theta \underline{x}}{3} \quad \text{and} \quad \underline{e}^{\mathrm{d}} = \underline{e} - \underline{e}^{\mathrm{i}},$$

where the arguments of the state functions and the vectors on which they operate are omitted for simplicity. For a spherical influence function the LPS model is isotropic (Silling et al., 2007, Proposition 14.1). In this model, K is the bulk modulus and α is proportional to the shear modulus G,

$$\alpha = \frac{15G}{m}. \tag{3.2}$$

We note that the LPS model is linear in the dilatation θ and in the deviatoric part of the extension $\underline{e}^{\mathrm{d}}$.

For a material with Poisson's ratio $\nu = 1/4$ the relation

$$G = \frac{3}{5}K \tag{3.3}$$

holds. In this case, (3.1) can be written as

$$\underline{t} = \frac{9K}{m} \underline{\omega}\, \underline{e}. \tag{3.4}$$

If we assume the specific spherical influence function

$$\underline{\omega}\, \langle \boldsymbol{\xi} \rangle = 1/\left|\left|\boldsymbol{\xi}\right|\right|, \tag{3.5}$$

then the weighted volume for a three-dimensional model is $m = \pi\delta^4$. Furthermore, the image of the extension scalar state can be written as

$$\underline{e}\, [\mathbf{x}, t]\, \langle \boldsymbol{\xi} \rangle = ||\boldsymbol{\xi}||\ \underline{s}\, [\mathbf{x}, t]\, \langle \boldsymbol{\xi} \rangle \tag{3.6}$$

with $\underline{s}$ the *stretch scalar state* defined by

$$\underline{s}\, [\mathbf{x}, t]\, \langle \boldsymbol{\xi} \rangle = \frac{||\boldsymbol{\xi} + \boldsymbol{\eta}|| - ||\boldsymbol{\xi}||}{||\boldsymbol{\xi}||}.$$

Substituting the above into (3.4) gives

$$\underline{t}\, [\mathbf{x}, t]\, \langle \boldsymbol{\xi} \rangle = \frac{1}{2} \left(\frac{18K}{\pi\delta^4} \right) s$$

with $s := \underline{s}\, [\mathbf{x}, t]\, \langle \boldsymbol{\xi} \rangle$. Utilizing (2.3) gives the bond-based model

$$f = c\, s \tag{3.7}$$

with $c = 18K/\pi\delta^4$. The model (3.7) is the prototype microelastic brittle (PMB) model.

Remark 3.1 *Utilizing the spherical influence function* (3.5)*, we have shown that the bond-based PMB model is a special case of the state-based LPS model, with Poisson's ratio* $\nu = 1/4$ *(by enforcing* (3.3)*). This relationship cannot be established using Boolean-valued influence functions that only select bonds, but instead requires an influence function that modulates the strength of nonlocal interactions.*

We now consider generalizations of the PMB model by varying the choice of influence function within the LPS model.

3.1 Generalized PMB models

We may derive generalized PMB (GPMB) models by restricting the Poisson's ratio in (3.1) to $\nu = 1/4$ (by enforcing (3.3)) and writing the influence function as

$$\underline{\omega}\,\langle\boldsymbol{\xi}\rangle = \omega_g(||\boldsymbol{\xi}||)\,||\boldsymbol{\xi}||^{-1}, \tag{3.8}$$

where $\omega_g(||\boldsymbol{\xi}||)$ is a general spherical function.[1] The resulting pairwise force function is

$$f = c_g\, s\, \omega_g(||\boldsymbol{\xi}||), \tag{3.9}$$

with corresponding pairwise potential function

$$w = \frac{1}{2} c_g\, s^2\, ||\boldsymbol{\xi}||\, \omega_g(||\boldsymbol{\xi}||). \tag{3.10}$$

Other generalizations of the PMB model have also been considered. In particular, a broad class of linearized GPMB models are analyzed in Zhou and Du (2010) and in Du and Zhou (2010).

The constant c_g depends upon the particular choice of $\omega_g(||\boldsymbol{\xi}||)$. We will define c_g by equating the macroelastic energy density of the GPMB model under an isotropic extension, i.e., $\boldsymbol{\eta} = r\boldsymbol{\xi}$ with r a constant, to the strain energy density in the classical theory of elasticity for the same material and the same deformation, $W = 9Kr^2/2$ (see Silling and Askari (2005)). This gives

$$\frac{1}{2}\int_{\mathcal{H}} w(\boldsymbol{\eta},\boldsymbol{\xi})dV_{\boldsymbol{\xi}} = \frac{1}{4} c_g\, r^2 \int_{\mathcal{H}} ||\boldsymbol{\xi}||\, \omega_g(||\boldsymbol{\xi}||)dV_{\boldsymbol{\xi}} = \frac{9Kr^2}{2},$$

from which we conclude

$$c_g = \frac{18K}{\displaystyle\int_{\mathcal{H}} ||\boldsymbol{\xi}||\, \omega_g(||\boldsymbol{\xi}||)dV_{\boldsymbol{\xi}}}. \tag{3.11}$$

By applying (2.3) to the state-based LPS model (3.4), we recover the bond-based GPMB model (3.9):

$$\underline{t}\,[\mathbf{x},t]\,\langle\boldsymbol{\xi}\rangle = \frac{9K}{m\,[\mathbf{x}]}\underline{\omega}\,\langle\boldsymbol{\xi}\rangle\ \underline{e}\,[\mathbf{x},t]\,\langle\boldsymbol{\xi}\rangle = \frac{9K}{\displaystyle\int_{\mathcal{H}} ||\boldsymbol{\xi}||^2\,\underline{\omega}\,\langle\boldsymbol{\xi}\rangle\, dV_{\boldsymbol{\xi}}}\underline{\omega}\,\langle\boldsymbol{\xi}\rangle\, ||\boldsymbol{\xi}||\ \underline{s}\,[\mathbf{x},t]\,\langle\boldsymbol{\xi}\rangle = \frac{1}{2}\left(\frac{18K}{\displaystyle\int_{\mathcal{H}} ||\boldsymbol{\xi}||\,\omega_g(||\boldsymbol{\xi}||)dV_{\boldsymbol{\xi}}}\right) s\,\omega_g(||\boldsymbol{\xi}||).$$

We now observe that the strain energy densities of an LPS model and its GPMB specialization are identical under general deformations by assuming (3.3) and (3.8). Using (3.10), we calculate the macroelastic energy density of the GPMB model to be

$$\begin{aligned} W_{\text{GPMB}} &= \frac{1}{2}\int_{\mathcal{H}} w(\boldsymbol{\eta},\boldsymbol{\xi})dV_{\boldsymbol{\xi}} = \frac{1}{2}\int_{\mathcal{H}} \frac{1}{2} c_g\, s^2\, ||\boldsymbol{\xi}||\,\omega_g(||\boldsymbol{\xi}||)dV_{\boldsymbol{\xi}} = \frac{1}{4} c_g \int_{\mathcal{H}} \left(\underline{e}\,\langle\boldsymbol{\xi}\rangle\right)^2 \frac{\omega_g(||\boldsymbol{\xi}||)}{||\boldsymbol{\xi}||} dV_{\boldsymbol{\xi}} \\ &= \frac{1}{4}\frac{18K}{\displaystyle\int_{\mathcal{H}} ||\boldsymbol{\xi}||\,\omega_g(||\boldsymbol{\xi}||)dV_{\boldsymbol{\xi}}}\int_{\mathcal{H}} \left(\underline{e}\,\langle\boldsymbol{\xi}\rangle\right)^2 \underline{\omega}\,\langle\boldsymbol{\xi}\rangle\, dV_{\boldsymbol{\xi}} = \frac{1}{2}\frac{9K}{m}\int_{\mathcal{H}} \underline{\omega}\,\langle\boldsymbol{\xi}\rangle\,\left(\underline{e}\,\langle\boldsymbol{\xi}\rangle\right)^2 dV_{\boldsymbol{\xi}}, \end{aligned}$$

where relations (3.8) and (3.6) are used. The strain energy density of the LPS model is (see Silling et al. (2007))

$$\begin{aligned} W_{\text{LPS}} &= \frac{K\theta^2}{2} + \frac{\alpha}{2}\int_{\mathcal{H}} \underline{\omega}\,\langle\boldsymbol{\xi}\rangle\left(\underline{e}^{\,\mathrm{d}}\,\langle\boldsymbol{\xi}\rangle\right)^2 dV_{\boldsymbol{\xi}} = \frac{K\theta^2}{2} + \frac{1}{2}\frac{9K}{m}\int_{\mathcal{H}} \underline{\omega}\,\langle\boldsymbol{\xi}\rangle\left(\underline{e}\,\langle\boldsymbol{\xi}\rangle - \frac{\theta}{3}||\boldsymbol{\xi}||\right)^2 dV_{\boldsymbol{\xi}} \\ &= \frac{K\theta^2}{2} + \frac{1}{2}\frac{9K}{m}\int_{\mathcal{H}} \underline{\omega}\,\langle\boldsymbol{\xi}\rangle\left(\left(\underline{e}\,\langle\boldsymbol{\xi}\rangle\right)^2 - 2\underline{e}\,\langle\boldsymbol{\xi}\rangle\,\frac{\theta}{3}||\boldsymbol{\xi}|| + \frac{\theta^2}{9}||\boldsymbol{\xi}||^2\right) dV_{\boldsymbol{\xi}} \\ &= \frac{K\theta^2}{2} + \frac{1}{2}\frac{9K}{m}\int_{\mathcal{H}} \underline{\omega}\,\langle\boldsymbol{\xi}\rangle\left(\underline{e}\,\langle\boldsymbol{\xi}\rangle\right)^2 dV_{\boldsymbol{\xi}} - K\theta^2 + \frac{K\theta^2}{2} = \frac{1}{2}\frac{9K}{m}\int_{\mathcal{H}} \underline{\omega}\,\langle\boldsymbol{\xi}\rangle\left(\underline{e}\,\langle\boldsymbol{\xi}\rangle\right)^2 dV_{\boldsymbol{\xi}}, \end{aligned}$$

where relations (3.2) and (3.3) are used. We see that $W_{\text{GPMB}} = W_{\text{LPS}}$.

[1] We restrict the choice of $\omega_g(||\boldsymbol{\xi}||)$ to those functions where equations (3.11), etc. are well-defined.

4 One-Dimensional Examples

In §3, we showed that the bond-based PMB model is a special case of the state-based LPS model for a particular choice of Poisson's ratio and influence function. Moreover, we showed that there are many generalized PMB (GPMB) models obtainable by varying the influence function of the LPS model. In this section, we explore the role of the influence function through one-dimensional examples, demonstrating that a rich spectrum of behavior can be achieved. In particular, we present a parameterized family of influence functions and show that by varying this parameter we can elicit increasingly localized behavior from a nonlocal model by modulating the strength of the nonlocal interactions.

4.1 First Example

We define a family of p-dependent spherical functions containing a softening length $\epsilon > 0$ (Dehnen (2001)) as

$$\Psi_p(|\xi|) := \left(\frac{1}{|\xi| + \epsilon}\right)^p. \tag{4.1}$$

Inserting this specific family of functions into (3.8) defines an influence function $\underline{\omega}\langle \boldsymbol{\xi} \rangle$ and produces the pairwise force function of the form (3.9)

$$f(x, x+\xi) = \gamma_p s \Psi_p(|\xi|) = \frac{\gamma_p}{|\xi|} \left(u(x+\xi, t) - u(x, t)\right) \left(\frac{1}{|\xi| + \epsilon}\right)^p, \tag{4.2}$$

with associated pairwise potential function of the form (3.10)

$$w(x, x+\xi) = \frac{1}{2}\gamma_p s^2 |\xi| \Psi_p(|\xi|) = \frac{1}{2}\frac{\gamma_p}{|\xi|} \left(u(x+\xi, t) - u(x, t)\right)^2 \left(\frac{1}{|\xi| + \epsilon}\right)^p.$$

The constant γ_p is found, as before, by equating the macroelastic energy density of this GPMB model under an isotropic extension to the strain energy density in the classical theory of elasticity for the same material and one-dimensional deformation, $W = 9Kr^2/10$. This results in

$$\gamma_p = \frac{9K}{5} \frac{1}{\displaystyle\int_0^\delta \xi \left(\frac{1}{\xi + \epsilon}\right)^p d\xi}. \tag{4.3}$$

The bulk modulus K has units of energy per volume. By assuming the one-dimensional system is represented by a bar of unit cross sectional area, we find that the units of γ_p are of force $\times$ length^{p-2}.

4.1.1 Dispersion Relation for the First Example

We derive the dispersion relationship for model (4.2), assuming $b(x, t) = 0$, to explore the effects of the parameter p. The equation of motion for model (4.2) is (see (2.4))

$$\rho \ddot{u}(x, t) = \int_{-\delta}^{\delta} \frac{\gamma_p}{|\xi|} \left(u(x+\xi, t) - u(x, t)\right) \left(\frac{1}{|\xi| + \epsilon}\right)^p d\xi, \tag{4.4}$$

where the mass density ρ is assumed to be uniform. We substitute the plane wave $u(x, t) = e^{i(kx + \Omega_p t)}$ into (4.4) and obtain

$$\Omega_p^2(k) = 2\frac{\gamma_p}{\rho} \int_0^\delta \frac{1}{\xi} \left(1 - \cos(k\xi)\right) \left(\frac{1}{\xi + \epsilon}\right)^p d\xi. \tag{4.5}$$

Assuming $k\delta \ll 1$, we use Taylor series to get

$$\Omega_p^2(k) = \frac{9K}{5\rho} k^2 \left[1 - \frac{2}{4!}\frac{I_{\delta,\epsilon}(p, 3)}{I_{\delta,\epsilon}(p, 1)} k^2 + \frac{2}{6!}\frac{I_{\delta,\epsilon}(p, 5)}{I_{\delta,\epsilon}(p, 1)} k^4 + \dots\right], \tag{4.6}$$

with

$$I_{\delta,\epsilon}(p,n) := \int_0^\delta \xi^n \left(\frac{1}{\xi+\epsilon}\right)^p d\xi.$$

A plot of the dispersion relation $\Omega_p(k)$ corresponding to (4.5) for various values of p, assuming $K = 1$, $\rho = 1$, $\delta = 5$, and $\epsilon = 1$, is shown in Figure 4.1(a). We see that as p increases, the dispersion relation approaches a linear dispersion relationship from below.

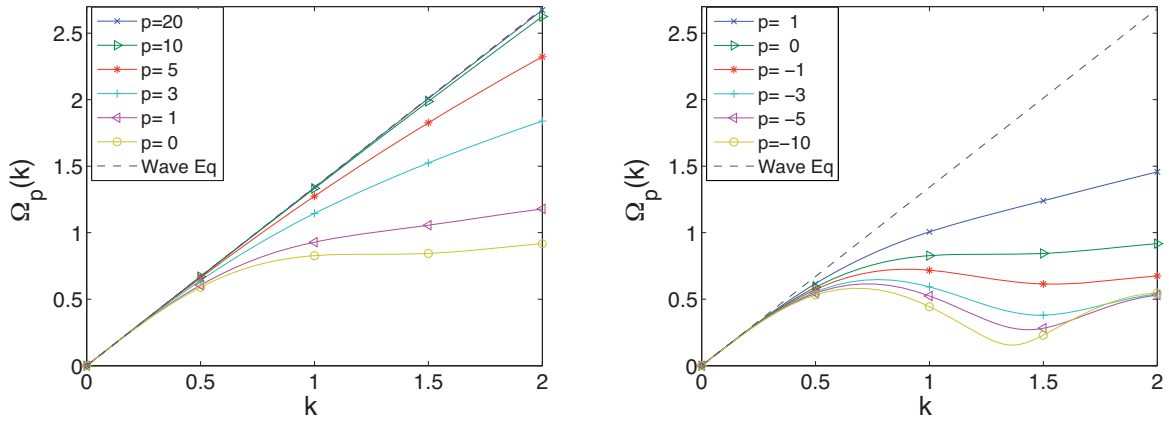

(a) First Example

(b) Second Example

Figure 4.1: Dispersion relations for various values of p, assuming $K = 1$, $\rho = 1$, and $\delta = 5$, for models (4.2) (with $\epsilon = 1$) and (4.9). The linear dispersion relation for the classical (local) wave equation is shown for comparison. In (a), we plot the dispersion relation corresponding to (4.5) (first example) and, in (b), the dispersion relation corresponding to (4.12) (second example).

4.1.2 Discretized Equation

Following Silling and Askari (2005), we discretize the domain into nodes separated by a uniform distance Δx in the reference configuration. Approximating the integral in (2.4) by a quadrature we obtain, for the one-dimensional model (4.2), the discretized equation of motion for node i

$$\rho \ddot{u}_i^n = \sum_{\substack{j=-N \\ j\neq 0}}^{N} \frac{\gamma_p}{|j\Delta x|} \left(u_{i+j}^n - u_i^n\right) \left(\frac{1}{|j\Delta x| + \epsilon}\right)^p \Delta x + b_i^n, \tag{4.7}$$

where $u_i^n = u(x_i, t_n)$, $b_i^n = b(x_i, t_n)$, ρ is a uniform density, and n is the time level. We assume $\delta = N\Delta x$ with N an integer, and observe that the constant γ_p depends on K, p, δ, and ϵ as defined in (4.3). We approximate $\ddot{u}_i^n$ by the centered finite difference

$$\ddot{u}_i^n \approx \frac{u_i^{n+1} - 2u_i^n + u_i^{n-1}}{\Delta t^2}$$

with Δt a constant time step. The system is evolved in time using the velocity Verlet algorithm.

4.1.3 Numerical Results

In this section, we present numerical results for the evolution of a smooth pulse in a one-dimensional system, for model (4.2), for different values of p. Following similar examples in Arndt and Griebel (2005), we choose

a domain $\mathcal{B} = [0, 1000]$. The initial profile is defined by $y(x, 0) = x + g(x)$ for all $x \in \mathcal{B}$, where $g(x)$ is a smooth 21-st order polynomial such that $g \equiv 0$ on $[0, 490] \cup [510, 1000]$, $g(500) = 1$, and $g'(x) = g''(x) = ... = g^{(10)}(x) = 0$ for $x = 490, 500, 510$. The one-dimensional grid has 4001 equally spaced nodes $\Delta x = 0.25$ apart. This mesh spacing with horizon $\delta = 5$ means that each node interacts with $N = 20$ neighboring nodes on each side. We choose bulk modulus $K = 1$, uniform density $\rho = 1$, horizon $\delta = 5$, softening length $\epsilon = 4\Delta x = 1$, time step $\Delta t = 0.1$ which is stable according to the Courant-Friedrichs-Lewy (CFL) condition, and time interval $[0, 220]$.

In Figure 4.2, we compare the density evolution for different values of p. The x-axis represents the reference configuration (the position of each node in the original grid) and the y-axis represents the time evolution (from top to bottom). The style used for these plots was borrowed from Arndt and Griebel (2005) and allows us to visualize an entire simulation evolution in a single figure. Each point in the plot corresponds to a given node at a specific time level. The color assigned to a point is a local approximation of the mass density $(dy/dx)^{-1}$, computed as $(x_{j+1} - x_{j-1})/(y_{j+1} - y_{j-1})$.

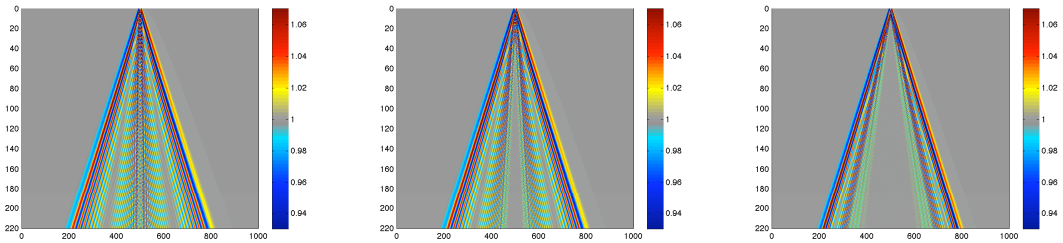

(a) $p = 0$ (b) $p = 1$ (c) $p = 3$

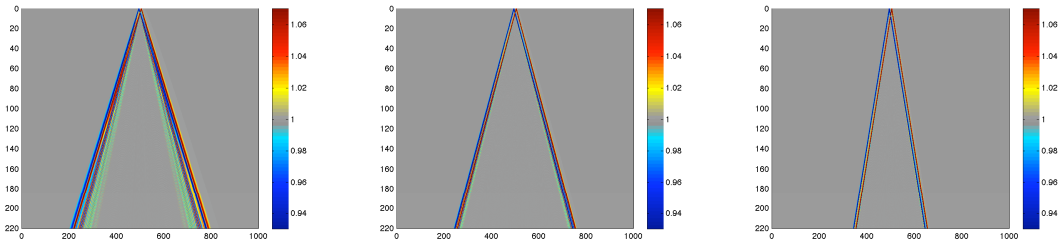

(d) $p = 5$ (e) $p = 10$ (f) $p = 20$

Figure 4.2: Density evolution for the peridynamic GPMB model (4.2), for different values of p. The x-axis represents the reference configuration, the y-axis represents the time evolution (from top to bottom), and the color assigned to a point represents the mass density. The style used for these plots was borrowed from Arndt and Griebel (2005). In these simulations, $K = 1$, $\rho = 1$, $\delta = 5$, $\epsilon = 4\Delta x = 1$, and $\Delta t = 0.1$. The larger the value of p, the slower the speed of propagation. Furthermore, the larger the value of p, the less dispersive the wave, where dispersion is numerically manifested as broadening of the lines. As p increases, the profile of the solution approaches the profile observed for the classical (local) wave equation (Seleson et al., 2009, Fig. 4.3(b)).

We observe that the wavespeed varies with p. We also notice that the larger the value of p, the less dispersive the wave, where dispersion is numerically manifested as broadening of the lines. Furthermore, as the value of p is increased, the profile of the solution approaches the profile observed for the classical (local) wave equation (Seleson et al., 2009, Fig. 4.3(b)).

We also note that the influence functions $\Psi_p(|\xi|)$ in (4.1), for $p = 0$ (Figure 4.3(a)) and $p = 1$ (Figure 4.3(b)), are qualitatively similar to constant and triangular micromodulus functions considered in Bobaru et al. (2009), respectively. The authors of that paper report that for the same value of δ, solutions computed

using the triangular micromodulus were closer to the classical (local) solutions than solutions computed using a constant micromodulus, which is consistent with our observations that increasingly local solutions are observed as p is increased.

In Figure 4.3, we present the profile of $\Psi_p(|\xi|)$ for the different values of p used for the simulations in Figure 4.2. As p increases, the relative weight of interactions carried by shorter bonds increases. The cross signs in the figures represent the values of $\Psi_p(|\xi|)$ at the locations of the nodes for the system corresponding to the simulations in Figure 4.2. We note that for the spatial discretization used, the discrete nonlocal model is well-approximated by a discrete local model for $p \approx 20$. This is consistent with the results in Figure 4.2.

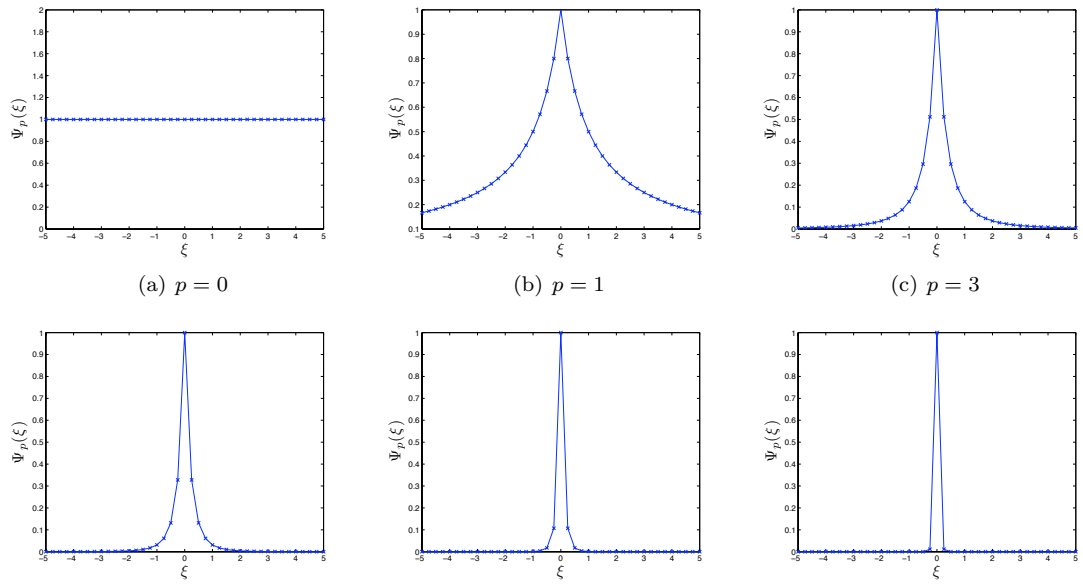

(a) $p = 0$ (b) $p = 1$ (c) $p = 3$

(d) $p = 5$ (e) $p = 10$ (f) $p = 20$

Figure 4.3: Comparison of $\Psi_p(|\xi|)$ in (4.1) for different choices of p, assuming $\epsilon = 1$. We used the same resolution as in Figure 4.2, i.e., $\Delta x = 0.25$. As p increases, the relative weight of interactions carried by shorter bonds increases.

To explain the results observed in Figure 4.2, we focus on the dispersion relation (4.6) for $\varepsilon = 1$ and $\delta = 5$. We compute the coefficients $\frac{2}{(n+1)!}\frac{I_{\delta,\varepsilon}(p,n)}{I_{\delta,\varepsilon}(p,1)}$ for different values of p and n to investigate the relative strength of the higher-order terms. In Table 4.1, we present these coefficients for different values of p. For large values of p, the coefficients of the higher-order terms decrease in magnitude and, in particular, for $p = 20$, the first higher-order term is three orders of magnitude smaller than the leading term. This explanation is consistent with our observation that our simulation results in Figure 4.2 approach those of a local model for large values of p.

Numerically, we note that for larger values of p, (say, $p = 20$), interactions are dominated by nearest neighbors (see Figure 4.3(f)). Using the discretization of §4.1.2, we note that for $p \gg 1$, we approach a limiting case where even nearest neighbor nodes are only loosely coupled.

4.2 Second Example

In the previous example, we saw that the influence function could be structured to weight more heavily the interactions carried by shorter bonds. A special case of particular interest is for the softening length $\varepsilon = 0$. In particular, this case has been analyzed in Zhou and Du (2010) and in Du and Zhou (2010). For this case,

Table 4.1: Values of the coefficients $\frac{2}{(n+1)!}\frac{I_{\delta,\varepsilon}(p,n)}{I_{\delta,\varepsilon}(p,1)}$ in (4.6), with $\varepsilon = 1$ and $\delta = 5$, for different values of p and n. For $p = 20$, we see that the magnitude of the coefficient corresponding to $n = 3$ in (4.6) is three orders of magnitude smaller than the leading term, i.e., $n = 1$.

p	$n=1$	$n=3$	$n=5$
0	1.00e+00	1.042e+00	5.787e-01
5	1.00e+00	1.225e-01	3.126e-02
20	1.00e+00	**1.838e-03**	5.836e-06
100	1.00e+00	5.369e-05	4.009e-09
1000	1.00e+00	5.035e-07	3.394e-13

we have a family of p-dependent spherical functions

$$\varphi_p(|\xi|) := \frac{1}{|\xi|^p}; \qquad p < 2.^2 \tag{4.8}$$

The corresponding pairwise force function of the form (3.9) is

$$f(x, x+\xi) = \beta_p\, s\, \varphi_p(|\xi|) = \beta_p\, (u(x+\xi,t) - u(x,t))\, \frac{1}{|\xi|^{p+1}}, \tag{4.9}$$

with associated pairwise potential function of the form (3.10)

$$w(x, x+\xi) = \frac{1}{2}\beta_p\, s^2\, |\xi|\, \varphi_p(|\xi|) = \frac{1}{2}\beta_p (u(x+\xi,t) - u(x,t))^2 \frac{1}{|\xi|^{p+1}}.$$

The functions (4.8) serve as a weighting of the strength of the bonds integrated within (2.4). For $p > 0$, shorter bonds have a higher relative weight, and for $p < 0$, longer bonds have a higher relative weight. Thus, this family of parameterized influence functions allows us to modulate the strength of nonlocal interactions, independently of the peridynamic horizon δ.

As in §4.1, the constant β_p is found by equating the macroelastic energy density of this GPMB model under an isotropic extension to the strain energy density in the classical theory of elasticity for the same material and one-dimensional deformation, $W = 9Kr^2/10$. The macroelastic energy density for an isotropic extension is

$$W = \frac{1}{2}\int_{\mathcal{H}} w d\xi = \frac{1}{2}\int_{-\delta}^{\delta} \frac{1}{2}\beta_p r^2\, |\xi|^{1-p}\, d\xi = \frac{1}{2}\beta_p r^2 \frac{\delta^{2-p}}{2-p}, \tag{4.10}$$

leading us to conclude

$$\beta_p = \frac{9K}{5}\frac{(2-p)}{\delta^{2-p}}. \tag{4.11}$$

For $p = 0$, (i.e., the PMB model (3.7)) we recover the result of Emmrich and Weckner (2006), $\beta_0 = 18K/5\delta^2$.

4.2.1 Dispersion Relation for the Second Example

As in §4.1.1, a dispersion relation can be derived for model (4.9) as

$$\Omega_p(k)^2 = \frac{18K}{5\rho}\frac{(2-p)}{\delta^{2-p}}\int_0^{\delta} (1 - \cos(k\xi))\, \frac{1}{\xi^{p+1}} d\xi. \tag{4.12}$$

[2]We assume $p < 2$ to avoid singularities in the macroelastic energy density calculation (4.10). For a more explicit quantification of acceptable choices for $\varphi_p(|\xi|)$, see Zhou and Du (2010).

Assuming $k\delta \ll 1$, we use Taylor series to get

$$\Omega_p(k)^2 = \frac{9K}{5\rho}k^2\left(1 - \frac{2}{4!}(k\delta)^2\frac{(2-p)}{(4-p)} + \frac{2}{6!}(k\delta)^4\frac{(2-p)}{(6-p)} + \dots\right).$$

So, the dispersion relation for $k\delta \ll 1$ is

$$\Omega_p(k) = \sqrt{\frac{9K}{5\rho}}k\sqrt{1 - \frac{2}{4!}(k\delta)^2\frac{(2-p)}{(4-p)} + \frac{2}{6!}(k\delta)^4\frac{(2-p)}{(6-p)} + \dots}.$$

An additional Taylor series expansion gives

$$\Omega_p(k) = \sqrt{\frac{9K}{5\rho}}k\left(1 - \frac{(2-p)}{4!(4-p)}(k\delta)^2 + \left(\frac{(2-p)}{6!(6-p)} - \frac{(2-p)^2}{2(4!)^2(4-p)^2}\right)(k\delta)^4 + \dots\right). \tag{4.13}$$

For $p = 0$,

$$\Omega_0(k) = \sqrt{\frac{9K}{5\rho}}k\left(1 - \frac{1}{48}(k\delta)^2 + \frac{17}{69120}(k\delta)^4 + \dots\right),$$

recovering the dispersion relation for the PMB model, (Seleson et al., 2009, Equation (4.9)).

Examining the dispersion relationship (4.13), we see that the magnitude of the higher-order terms increases as p decreases, suggesting model (4.9) is more dispersive with decreasing p. A plot of $\Omega_p(k)$ corresponding to (4.12) for various values of p, assuming $K = 1$, $\rho = 1$, and $\delta = 5$, is shown in Figure 4.1(b) and supporting numerical experiments appear in Figure 4.4.

4.2.2 Numerical Experiments

We present similar numerical experiments as for the first example, using the same domain, initial profile, grid, horizon, bulk modulus, density, time step, time interval, and an analogous discretization.

In Figure 4.4, we compare the density evolution for different values of p. The axis and color interpretations are the same as in Figure 4.2.

From Figure 4.4 we observe that more negative values of p apparently produce more dispersive interactions, where dispersion is numerically manifested as broadening of the lines. This observation is in agreement with the nonlinear dispersion relation (4.13). Furthermore, the velocity of propagation is dependent upon p. As we can see from the slopes at the wavefronts, the velocity of the leading mode increases as p decreases.

5 Three-Dimensional Examples

To investigate the effect of the influence function on the evolution of fracture patterns, we utilized the PDLAMMPS (peridynamics-in-LAMMPS) code (Parks et al., 2008)[3], and modified it to include the spherical function (5.2). The GPMB pairwise force function implemented in the PDLAMMPS code has the form

$$\mathbf{f}(\boldsymbol{\eta}, \boldsymbol{\xi}) = \gamma_p^{(3d)}\, s(\boldsymbol{\eta}, \boldsymbol{\xi})\Psi_p(||\boldsymbol{\xi}||)\,\frac{\boldsymbol{\xi} + \boldsymbol{\eta}}{||\boldsymbol{\xi} + \boldsymbol{\eta}||} \tag{5.1}$$

with s the stretch (see §3) and

$$\Psi_p(||\boldsymbol{\xi}||) := \left(\frac{1}{||\boldsymbol{\xi}|| + \epsilon}\right)^p. \tag{5.2}$$

[3]Available at `http://lammps.sandia.gov`.

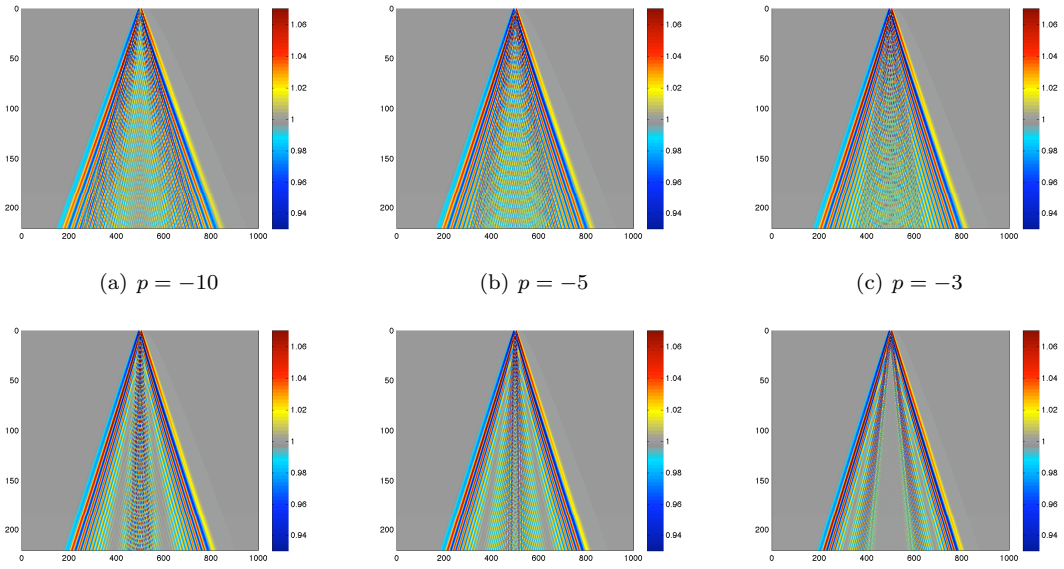

(a) $p = -10$ (b) $p = -5$ (c) $p = -3$

(d) $p = -1$ (e) $p = 0$ (f) $p = 1$

Figure 4.4: Density evolution of the peridynamic GPMB model (4.9) for different values of p. The axis and color interpretations are the same as in Figure 4.2. The $p = 1$ case is the least dispersive, where dispersion is numerically manifested as broadening of the lines. Further, the slope at the wavefront indicates that the velocity of the leading mode increases as p decreases.

As in (3.11), we find the expression for the constant $\gamma_p^{(3d)}$ to be

$$\gamma_p^{(3d)} = \frac{18K}{\displaystyle\int_{\mathcal{H}} ||\boldsymbol{\xi}|| \left(\frac{1}{||\boldsymbol{\xi}|| + \epsilon}\right)^p dV_{\boldsymbol{\xi}}}.$$

In order to simulate fracture, we assume bonds break if they are stretched too far. This "critical stretch" is determined from the strain energy release rate for brittle fracture, see Silling and Askari (2005) for details. Once bonds are broken, they remain broken. In the following figures we will plot the damage as the simulation proceeds. The damage at a point is computed as one minus the number of unbroken bonds in the current configuration divided by the number of unbroken bonds in the reference configuration, see Parks et al. (2008) for further details. Thus, a damage of zero corresponds to pristine material, and the maximum sustainable damage is one.

Following Silling and Askari (2005), we simulate the impact of a hard sphere on a brittle target with free boundary conditions. The target is a thin disc of diameter 74 mm and height 2.5 mm, modeled with the GPMB material (5.1), and having bulk modulus $K = 14.9$ GPa and density $\rho = 2200\,\mathrm{kg/m^3}$. The spherical projectile has a radius of 10 mm and a velocity of 100 m/s. The target is discretized using a cubic lattice with lattice constant $a = 0.5$ mm, giving a total of about $103,000$ particles, and the horizon is chosen as $\delta = 3a = 1.5$ mm. We choose a softening length $\epsilon = a = 0.5$ mm. The time step is chosen as $\Delta t = 10^{-9}$ s, which is CFL-stable. We investigate fracture patterns for the cases $p = 0, 3, 5, 10$. The values for the constant $\gamma_p^{(3d)}$, for the different values of p, are given in Table 5.1. In Figure 5.1, top-down views of the target are shown for various time instants during the simulation, with the projectile removed so as to not obscure the target. We observe that the cracks in Figures 5.1(j,k,l) grow essentially along the axes of the mesh, whereas the cracks in Figures 5.1(a,b,c) appear to be independent of the mesh. Similar mesh-dependent crack growth was observed in Parks et al. (2008) for small values of the horizon δ. This is consistent with the hypothesis

that large values of p lead to models dominated by local and nearly-local interactions.

In Figure 5.2, the target is a cylinder of diameter 34 mm and height 25 mm. The same material, boundary conditions, and spatial discretization as in Figure 5.1 are assumed, giving about $185,000$ particles. The projectile has the same radius as in the previous example, but an impact velocity of 35 m/s is chosen, which produces Hertzian cracks (Silling and Askari (2005)). The time step is chosen to be $\Delta t = 10^{-8}$ s, which is CFL-stable. In Figure 5.2, snapshots of a cut view of the cylinder are shown at different time instants, with the projectile again hidden so as to not obscure the target. Hertzian cracks are observed to form for small values of p, e.g., $p = 0$; this is qualitatively similar to results presented in Silling and Askari (2005). In contrast, for large values of p, e.g., $p = 10$, the Hertzian crack essentially disappears. Furthermore, it appears that the angle of propagation of the Hertzian crack is dependent upon p. Particularly, for large values of p, e.g., $p = 10$, the fracture propagates faster towards the bottom of the cylinder, producing more damage at the base of the target.

Table 5.1: Values for $\gamma_p^{(3d)}$ (in units of $\mathrm{N\,m}^{p-6}$) for different values of p.

p	$\gamma_p^{(3d)}$
0	$1.6863 \cdot 10^{22}$
3	$6.8586 \cdot 10^{13}$
5	$1.3491 \cdot 10^{8}$
10	$1.6977 \cdot 10^{-7}$

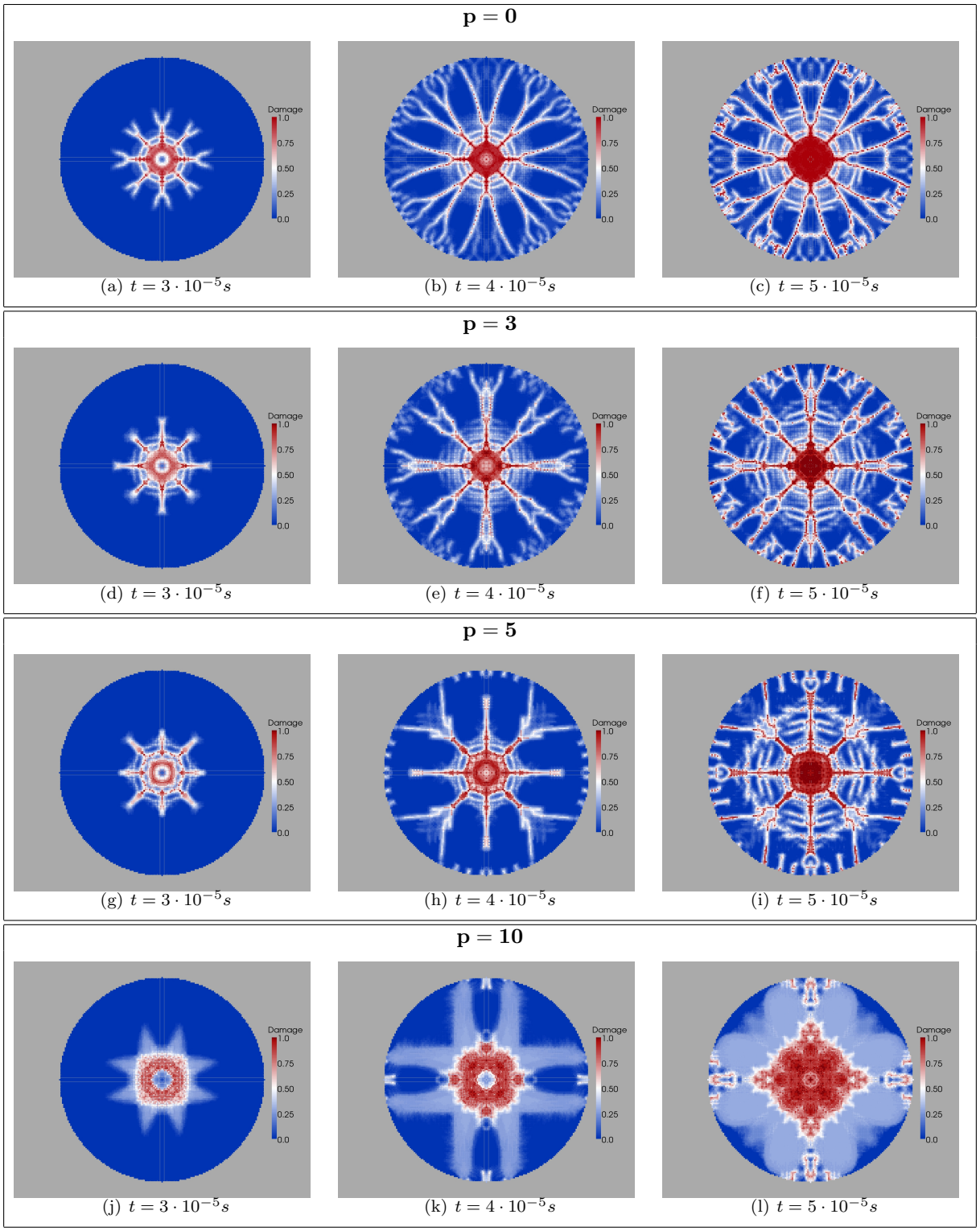

(a) $t = 3 \cdot 10^{-5}s$ (b) $t = 4 \cdot 10^{-5}s$ (c) $t = 5 \cdot 10^{-5}s$

(d) $t = 3 \cdot 10^{-5}s$ (e) $t = 4 \cdot 10^{-5}s$ (f) $t = 5 \cdot 10^{-5}s$

(g) $t = 3 \cdot 10^{-5}s$ (h) $t = 4 \cdot 10^{-5}s$ (i) $t = 5 \cdot 10^{-5}s$

(j) $t = 3 \cdot 10^{-5}s$ (k) $t = 4 \cdot 10^{-5}s$ (l) $t = 5 \cdot 10^{-5}s$

Figure 5.1: Top-down views of the impact of a hard sphere (not shown) on a disc of brittle material, for different time instants (left to right), for the GPMB model (5.1) (using (5.2)) with $\varepsilon = a$, $\delta = 3a$ and a is the grid size, for $p = 0$ (a,b,c), 3 (d,e,f), 5 (g,h,i), 10 (j,k,l). The discs are colored by damage with blue representing 0% damage and red representing 100% damage.

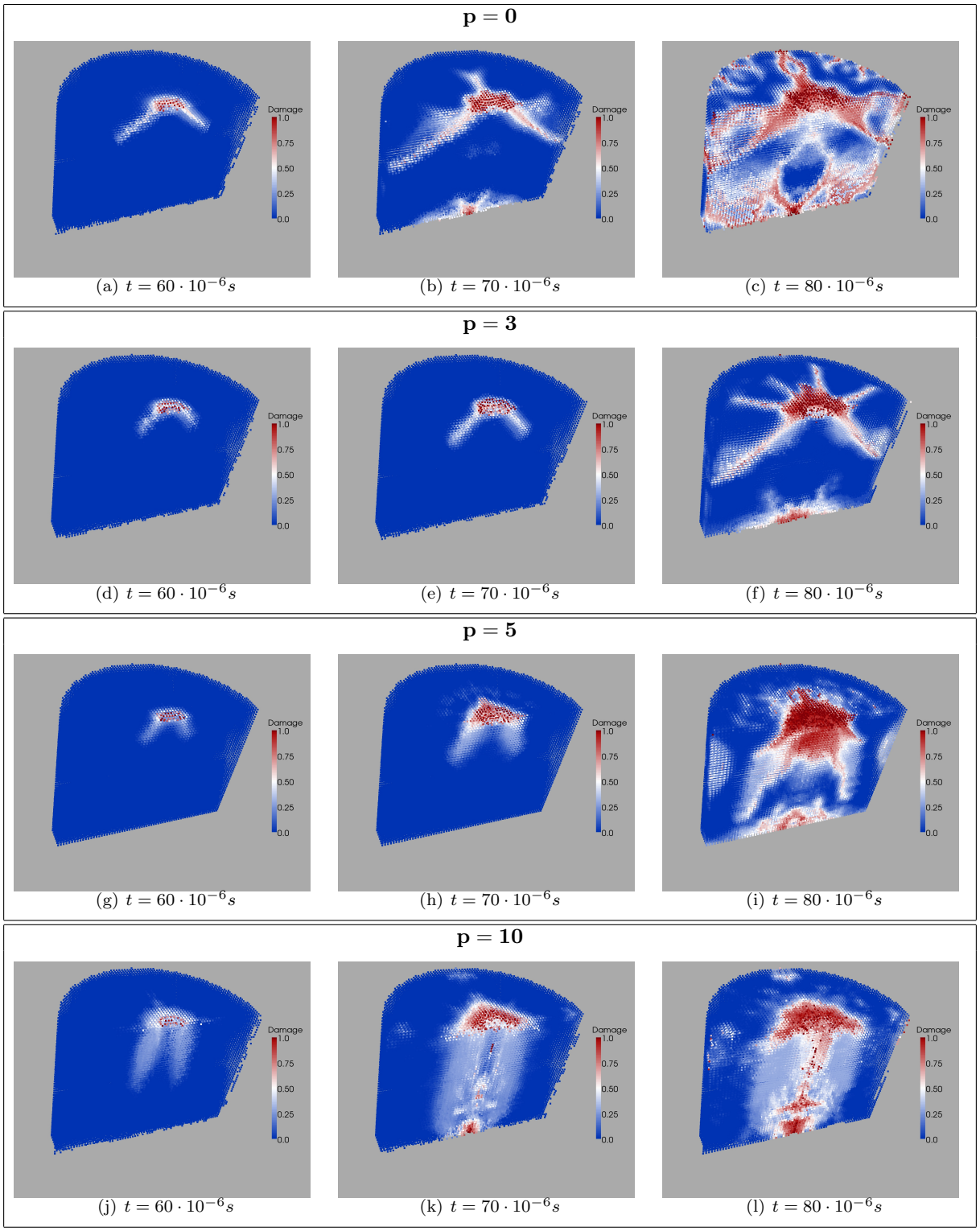

Figure 5.2: Cut views of the impact of a hard sphere (not shown) on a cylinder of brittle material, for different time instants (left to right), for the GPMB model (5.1) (using (5.2)) with $\varepsilon = a$, $\delta = 3a$ and a is the grid size, for $p = 0$ (a,b,c), 3 (d,e,f), 5 (g,h,i), 10 (j,k,l). The cylinders are colored by damage with blue representing 0% damage and red representing 100% damage.

6 Conclusions

To explore the role of influence functions within the peridynamic theory, we began by demonstrating that the bond-based PMB model (3.7), the most popular bond-based peridynamic model, is a special case of the state-based LPS model (3.1), for Poisson's ratio $\nu = 1/4$ and influence function (3.5). We also showed that there exists a related family of generalized PMB (GPMB) models that can be derived by selecting other influence functions. Using one-dimensional examples, we explored two specific choices of influence functions based upon (4.1) and (4.8), showing that influence functions can be used to control nonlocal effects within a peridynamic model independently of the peridynamic horizon, δ. Lastly, we investigated the effect specific influence functions have on dynamic fracture simulations, reporting results for the impact of a hard sphere on two different brittle targets.

The application of influence functions in peridynamics represents an entirely new and essentially unexplored facet of nonlocal modeling. Influence functions enable a rich spectrum of behavior in nonlocal dynamical systems, even when the peridynamic horizon is fixed. Increasing (or decreasing) the peridynamic horizon increases (or decreases) the size of the neighborhood $\mathcal{H}_{\mathbf{x}}$ in (2.1) and thus the number of bonds $\mathbf{x}' - \mathbf{x}$. The influence function modulates how these bonded points interact. Only simple examples of influence functions were presented in this paper, and their potential full impact has just begun to be explored.

Acknowledgement

This work was supported by the Laboratory Directed Research and Development program at Sandia National Laboratories. The first author also recognizes support from DOE/OASCR under grant number DE-FG02-05ER25698. The authors acknowledge several insightful discussions with Stewart Silling (Sandia), Max Gunzburger (Florida State), Rich Lehoucq (Sandia), and Per Arne Rikvold (Florida State). The authors thank the Florida State University shared High-Performance Computing facility and staff for assistance with the 3D fracture simulations. The authors also acknowledge helpful comments from the two anonymous referees.

References

Aksoylu, B. and Parks, M. L., 2009. Towards domain decomposition for nonlocal problems. Technical Report SAND2009-6228J, Sandia National Laboratories.

Alali, B., 2008. *Multiscale Analysis of Heterogeneous Media for Local and Nonlocal Continuum Theories*. Ph.D. thesis, Louisiana State University.

Arndt, M. and Griebel, M., 2005. Derivation of higher order gradient continuum models from atomistic models for crystalline solids. *Multiscale Model. Simul.*, 4, 531–562.

Askari, E., Bobaru, F., Lehoucq, R. B., Parks, M. L., Silling, S. A., and Weckner, O., 2008. Peridynamics for multiscale materials modeling. In *SciDAC 2008, 13-17 July, Washington*, volume 125 of *J. Phys.: Conf. Ser.*, page 012078. IOP Publishing.

Bobaru, F., Yang, M., Alves, L. F., Silling, S. A., Askari, E., and Xu, J., 2009. Convergence, adaptive refinement, and scaling in 1D peridynamics. *Int. J. Numer. Meth. Engng.*, 77, 852877.

Dehnen, W., 2001. Towards optimal softening in three-dimensional N-body codes - I. Minimizing the force error. *Mon. Not. R. Astron. Soc.*, 324, 273–291.

Du, Q. and Zhou, K., 2010. Mathematical analysis for the peridynamic nonlocal continuum theory. *ESAIM: M2AN*. To appear.

Emmrich, E. and Weckner, O., 2006. The peridynamic equation of motion in non-local elasticity theory. *III European Conference on Computational Mechanics; Solids, Structures and Coupled Problems in Engineering; C.A.Mota Soares et al. (eds.); Lisbon, Portugal, 5-8 June 2006*.

Emmrich, E. and Weckner, O., 2007. On the well-posedness of the linear peridynamic model and its convergence towards the Navier equation of linear elasticity. *Commun. Math. Sci.*, 5, 4, 851–864.

Eringen, A. C., 2002. *Nonlocal Continuum Field Theories*. Springer, New York.

Foster, J. T., Silling, S. A., and Chen, W. W., 2010. Viscoplasticity Using Peridynamics. *Int. J. Numer. Meth. Engng.*, 81, 1242–1258.

Gunzburger, M. and Lehoucq, R. B., 2010. A nonlocal vector calculus with application to nonlocal boundary value problems. *Multiscale Model. Simul.*, 8, 5, 1581–1598.

Ha, Y. D. and Bobaru, F., 2010. Studies of dynamic crack propagation and crack branching with peridynamics. *Int J. Fract.*, 162, 229–244.

Kröner, E., 1967. Elasticity theory of materials with long range cohesive forces. *Internat. J. Solids Structures*, 3, 5, 731–742.

Kunin, I. A., 1982. *Elastic media with microstructure I: One-dimensional models*, volume 26 of *Springer Series in Solid State Sciences*. Springer-Verlag, Berlin.

Kunin, I. A., 1983. *Elastic media with microstructure II: Three-dimensional models*, volume 44 of *Springer Series in Solid State Sciences*. Springer-Verlag, Berlin.

Love, A. E. H., 1944. *A Treatise on the Mathematical Theory of Elasticity*. Dover, 4th edition.

Parks, M. L., Lehoucq, R. B., Plimpton, S. J., and Silling, S. A., 2008. Implementing peridynamics within a molecular dynamics code. *Comp. Phys. Comm.*, 179, 11, 777–783.

Rogula, D., 1982. Introduction to nonlocal theory of material media. In D. Rogula, editor, *Nonlocal Theory of Material Media*, pages 125–222. Springer-Verlag, Berlin.

Seleson, P., Gunzburger, M., and Parks, M. L., 2010. Coupling local and nonlocal diffusion models across interfaces. In Preparation.

Seleson, P., Parks, M. L., Gunzburger, M., and Lehoucq, R. B., 2009. Peridynamics as an Upscaling of Molecular Dynamics. *Multiscale Model. Simul.*, 8, 1, 204–227.

Silling, S. A., 2000. Reformulation of elasticity theory for discontinuities and long-range forces. *J. Mech. Phys. Solids*, 48, 175–209.

Silling, S. A. and Askari, E., 2005. A meshfree method based on the peridynamic model of solid mechanics. *Computers and Structures*, 83, 1526–1535.

Silling, S. A., Epton, M., Weckner, O., Xu, J., and Askari, E., 2007. Peridynamic States and Constitutive Modeling. *J. Elasticity*, 88, 151–184.

Zhou, K. and Du, Q., 2010. Mathematical and numerical analysis of linear peridynamic models with nonlocal boundary conditions. *SIAM J. Num. Anal.*. To appear.